LONG-TERM LAND SURFACE WATER MONITORING IN THE YELLOW RIVER BASIN OF CHINA BASED ON LANDSAT IMAGERY ON THE GOOGLE EARTH ENGINE

Hongye Cao[a], Ling Han[b,*], Liangzhi Li[a]

[a] *College of Geological Engineering and Geomatics, Chang'an University, Xi'an 710064, China*

[b] *School of Land Engineering, Chang'an University, Xi'an 710064, China*

*Corresponding author:

E-mail address: hanling@chd.edu.cn (L. Han).

Commission III, WG III/1

KEY WORDS: surface water, Landsat TM, Landsat ETM+, Landsat OLI, Google Earth Engine, Yellow River Basin.

ABSTRACT:

Land surface water is the most active part of the earth's surface layer and plays an important role in material balance and energy transformation. The monitoring of dynamic changes in surface open water helps to grasp the distribution and changes of water resources, which is important for understanding the impact of human activities on water resources and safeguarding the ecological security of the basin. In the study, 72,520 Landsat images were processed using the Google Earth Engine (GEE) cloud platform to study the long-term changes of the open surface water in the Yellow River Basin (YRB) from 2000 to 2020. The results show that (1) The multi-index water body extraction rules (MIWER) is suitable for long-term and large-scale surface water mapping based on Landsat images; (2) From 2000 to 2020, both permanent and seasonal water in the whole YRB and sub-basins have increased. In general, the total open surface water in the YRB show an increasing trend with obvious spatial heterogeneity; (3) The changes of open surface water in the YRB are related to climate change and intensive human activities, but the influencing factors vary in different regions and need to be further studied in the future. The findings of this study can be used to help the policy-makers understand changing water resources and their driving mechanism and provide a reference for water resources management, agricultural irrigation, and ecological protection.

1. INTRODUCTION

The hydrosphere is the supplier of the Earth's water cycle and an important mediator of material transport and energy exchange between the atmosphere, lithosphere, and biosphere, contributing to the integrity of the geographic environment (Kang et al., 2007). Among them, surface water, an important component of the hydrosphere, is a valuable water resource for humans, providing a wide range of services such as industrial and agricultural production, regional climate regulation and ecosystem maintenance (Pekel et al., 2016; Vörösmarty et al., 2010). Surface water plays an indispensable role in the hydrological and biogeochemical cycles at local, national, and global scales (Wang et al., 2019). However, with global warming and drought, water pollution and water shortage have become two major problems to be solved in water resources conservation. Long-term monitoring of surface water, analyzing their dynamic changes, and proposing corresponding solutions can provide a theoretical basis for rational development, utilization, and protection of water resources (Cao et al., 2021; Che et al., 2019).

Remote sensing technology has the advantages of wide coverage and high timeliness and is used in resource surveys (Avtar et al., 2020), environmental evaluation (Lloyd et al., 2018; Zhang et al., 2011), urban research (Li 2021), disaster monitoring (Cao et al., 2021; Jacobs et al., 2019; Rudorff et al., 2018) and other fields have achieved wide applications. At present, remote sensing technologies are making great progress, such as the continuous improvement of optical remote sensing and microwave radar, the increased spatial resolution of remote sensing data, and the extraction algorithms of water bodies. These provide technical support for the accurate and rapid extraction of surface water bodies as well as dynamic monitoring.

Currently, the main methods for water extraction are the index threshold method and classification method. Classification methods mainly use a series of predictor variables, including original spectral bands and water indices, to build a classification model, which in turn distinguishes water bodies from non-water bodies. Common classification models include support vector machine (SVM) (Meng et al., 2019), maximum likelihood (ML) (Jay et al., 2014), random forest (RF) (Rao et al., 2018), etc. For these classification models, the accuracy of the model is influenced by the training samples, predictor variables, and model parameters. In addition, classification models often require more time to produce classification results. Water index threshold methods are widely used to extract surface water bodies, and these common water indices include the Normalized Difference Water Index (NDWI) (McFeeters 1996), Modified Normalized Difference Water Index (MNDWI) (Xu 2006), and Automatic Water Extraction Index (AWEI) (Feyisa et al., 2014). However, the ideal single threshold for distinguishing water bodies from non-water bodies is difficult to determine due to the varying spatial and temporal characteristics of the spectra of water bodies (Cui et al., 2012). A detection rule combining multiple water body indices can extract surface water bodies with high accuracy and efficiency. However, this detection rule is rarely used to extract surface water at present. Therefore, there is an urgent need to develop new water

detection rules to grasp the distribution and change of surface resources in YRB.

In this study, we integrated all the available time-series Landsat images (TM/ETM+/OLI) of China during 2000 to 2020 in GEE to: (1) develop a simple but robust method to map surface water; (2) apply this method to generate maps of surface water in China during 2000 to 2020 based on the GEE platform and Landsat historical images; (3) analyze the spatial distribution of surface water in YRB from 2000 to 2020.

2. MATERIALS AND METHODS

2.1 Study area

The YRB is situated in northern China (30–42°N, 94–120°E; Figure 1) with a total area of up to 7.95 × 10^5 km^2; it is one of the most important basins in China and is formed by the Yellow River, which is the second-largest river in China, second only to the Yangtze River. Based on topographic variations (high in the west and low in the east), the YRB is usually divided into upper (UYRB), middle (MYRB), and lower reaches (LYRB). From the source of the Yellow River (point A in Figure 1) in the Bayankara Mountains at about 4,800 m above sea level, it descends to Hekou County at 1,000 m (B), Zhengzhou City at 400 m (C), and finally flows to the Bohai Sea (D) (Figure 1). The upper reaches receive water from melting glaciers on the Tibetan plateau. Due to the different altitudes between the upper and middle reaches, the middle reaches of the Loess Plateau and Ordos Plateau have poor land and severe water erosion; the lower reaches consist of alluvial plains, which are suitable for growing crops, high population density, and dense urban areas. However, the lower reaches suffer the most from flood disasters.

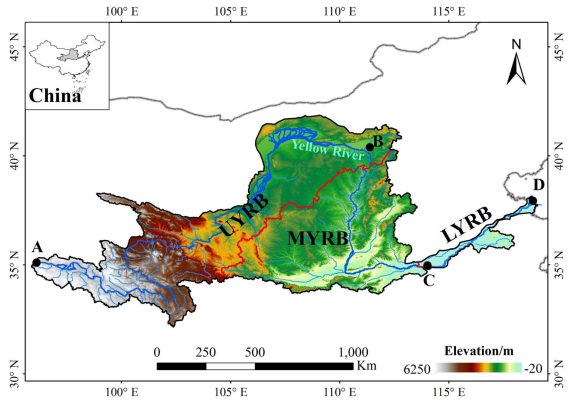

Figure 1. Yellow River Basin, the study area. The red line delineates three areas (UYRB: upper reaches of the Yellow River Basin; MYRB: middle reaches of the Yellow River Basin; LYRB: lower reaches of the Yellow River Basin). A continuous blue bolded curve shows the Yellow River, which passes from the Tibetan Plateau through the Alashan Plateau, the Ordos Plateau, and the Loess Plateau before finally joining the Bohai Sea. Points A, B, C, and D are the key points of the Yellow River. B is the dividing point between upstream and midstream, and C is the dividing point between midstream and downstream.

2.2 Data and processing

The YRB area is covered with 74 tiles (path/row) of the Landsat Worldwide Reference System (WRS-2) (Figure 2 (a)). We acquired a total of 72,520 Landsat surface reflectance images (21,312 Landsat 5 images, 37,296 Landsat 7 images, and 13,912 Landsat 8 images) for all available Landsat images in the GEE platform from January 1, 2000, to December 31, 2020. Surface reflectance datasets for Landsat 5 and 7 were generated by the Landsat Ecosystem Disturbance Adaptive Processing System (LEDAPS) algorithm (Claverie et al., 2015), and the Landsat 8 surface reflectance products were generated by the Landsat Surface Reflectance Code (LaSRC) algorithm (Vermote et al., 2016). In this study, six spectral bands of Landsat series images, such as blue band, green band, red band, near-infrared band, short-wave infrared band 1 (SWIR1), and short-wave infrared band 2 (SWIR2) with a spatial resolution of 30 m, were used for extracting water bodies.

We used the Cloud_Cover score in the Landsat metadata to remove images with high cloud cover, and used the Landsat quality assessment (QA) band (pixel_qa) to mark observations with poor quality (e.g., clouds and cloud shadows) for each image. In addition, we used the Shuttle Radar Topography Mission (SRTM) Digital Elevation Model (DEM) (Farr et al., 2007), the solar azimuth, and the zenith angle of each image, and the ee.Terrain.hillShadow algorithm in GEE to identify and remove terrain shadows (Zou et al., 2018). Ultimately, 26,681 high-quality Landsat images (7,288 Landsat 5 images, 13,987 Landsat 7 images, and 5,406 Landsat 8 images) were generated for the study area, and the temporal (year and month) and spatial distribution of these data are shown in Figure 2.

In addition, Sentinel-2 images with a spatial resolution of 10 m were used to assess the accuracy of the water bodies extracted in the YRB. The study shows that high spatial resolution image data can be used to validate low-resolution image data for extracting feature information. ERA5 is the fifth generation ECMWF (European Centre for Medium-Range Weather Forecasts) atmospheric reanalysis of the global climate (Urban et al., 2021). Reanalysis combines model data with observations from across the world into a globally complete and consistent dataset. To analyze the temporal trends of precipitation in the YRB, annual and monthly ERA5 precipitation products with a spatial resolution of 0.25° were collected for the period from 2000 to 2020. In addition, GlobalLand30 (Global 30-meter land cover remote sensing data product) data (http://www.globallandcover.com/) and SRTM DEM data (https://srtm.csi.cgiar.org/srtmdata/) were collected to show the land cover and elevation of the YRB.

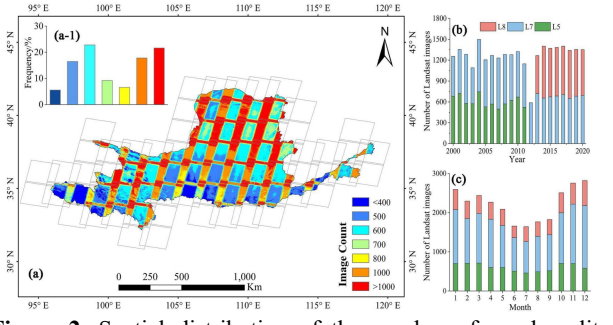

Figure 2. Spatial distribution of the number of good-quality observations within individual pixels of Landsat 5/7/8 images from 2000 to 2020 and Landsat WRS-2 path/rows (gray boxes) in the study area (a). Annual (b) and monthly (c) distribution of the number of good-quality observations of Landsat 5/7/8 images from 2000 to 2020.

2.3 Sample Collection

Surface reflectance exhibits intra-annual variability due to differences in feature and sun angles (Zhu et al., 2015). D'Odorico et al., (2013) showed that the percentile synthesis method can be used to generate images of seasonal variability. In statistics, a percentile is a score below which a given percentage of scores in its frequency distribution falls (exclusive definition) or a score at or below which a given percentage falls

(inclusive definition) (Yu et al., 2021). In this study, the percentile synthesis method was used to obtain images of seasonal changes in the study area.

First, among the 74 Landsat tiles covering the entire YRB area, 10 tiles representing different land cover types were randomly selected, as shown in Figure 3. These tiles cover typical surface open water bodies in the YRB region, such as high-elevation lakes (e.g. Zhaling Lake), high-elevation rivers and reservoirs (e.g. Longyangxia Reservoir), low-elevation lakes (e.g. Wulangsu Sea), low-elevation rivers and reservoirs (e.g. Qianhe Reservoir), plain lakes (e.g. Dongping Lake), and plain rivers and reservoirs (e.g. Xiaolangdi Reservoir); then, all images from 2000 to 2020 in each tile were combined into one image collection and the surface reflectance percentages in each band were calculated for each pixel in each image collection; finally, six single spectral bands (blue band, green band, red band, near-infrared band, short-wave infrared band 1, and short-wave infrared band 2) in each image collection were synthesized into one multispectral image. Percentile synthetic images ranging from 10% to 90% were calculated for each tile in this study.

As shown in Figure 3, observing the different percentile images representing the Hongjiannao Lake(Landsat tile No. 127033) and Xiaolangdi Reservoir (Landsat tile No. 125036), it is easy to find that the percentile images show a more significant seasonal variation, i.e., the lower percentile has a greater chance of representing surface water bodies. The 90% percentile synthetic images in this study represent the minimum range of surface water pixels for randomly generated water body samples, and the 10% percentile synthetic image set represents the minimum range of non-surface water pixels for randomly generated non-water body samples. A total of 685,445 samples, including 252,832 water samples and 432,613 non-water samples, were collected in this study and used to establish water extraction rules.

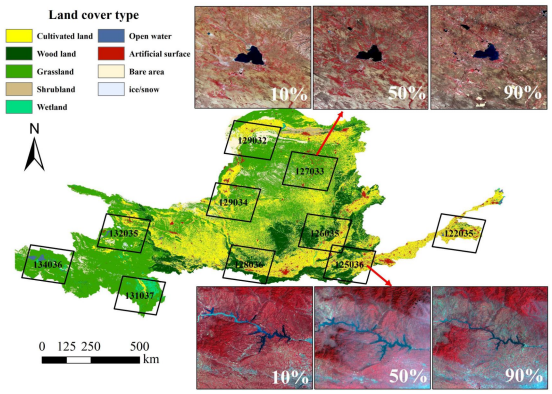

Figure 3. Spatial distribution of sampled tiles and composite images of the three percentiles (10%, 50%, and 90%) (false color shows RGB: NIR, Red, Green). The numbers in the sampled plots indicate the paths (first three digits) and rows (last three digits) of Landsat WRS-2. The land cover type data are from GlobalLand30.

2.4 Surface Water Extraction Algorithm

The MNDWI (modified normalized difference water index), AWEI (automated water extraction index), EVI (enhanced vegetation index), and NDVI (normalized differential vegetation index) index were used to develop a multi-index water body extraction rules (MIWER). The pixels are water bodies when the pixels satisfy (*MNDWI - EVI* > -0.1 or *MNDWI – NDVI* > -0.1) and ($AWEI_{nsh} - AWEI_{sh}$ > -0.1); otherwise, they are the non-water body. 0.5% of water samples were incorrectly classified as non-water bodies and 3.45% of non-water samples were incorrectly classified as water bodies in the scatter density figure (Figure 4) of all sample points.

$$MNDWI = \frac{\rho_{Green} - \rho_{SWIR1}}{\rho_{Green} + \rho_{SWIR1}} \quad (1)$$

$$\begin{aligned} AWEI_{nsh} &= 4 \cdot (\rho_{Green} - \rho_{SWIR1}) - (0.25 \cdot \rho_{NIR} + 2.75 \cdot \rho_{SWIR2}) \\ AWEI_{sh} &= \rho_{Blue} + 2.5 \cdot \rho_{Green} - 1.5 \cdot (\rho_{NIR} + \rho_{SWIR1}) - 0.25 \cdot \rho_{SWIR2} \end{aligned} \quad (2)$$

$$EVI = 2.5 \cdot \frac{\rho_{NIR} - \rho_{Red}}{\rho_{NIR} + 6 \cdot \rho_{Red} - 7.5 \cdot \rho_{Blue} + 1} \quad (3)$$

$$NDVI = \frac{\rho_{NIR} - \rho_{Red}}{\rho_{NIR} + \rho_{Red}} \quad (4)$$

Here, ρ_{Red}, ρ_{Green}, ρ_{Blue}, ρ_{NIR}, ρ_{SWIR1} and ρ_{SWIR2} are the reflectance of the red band, green band, blue band, near-infrared band 1, shortwave infrared band 1 and 2 of Landsat image, respectively.

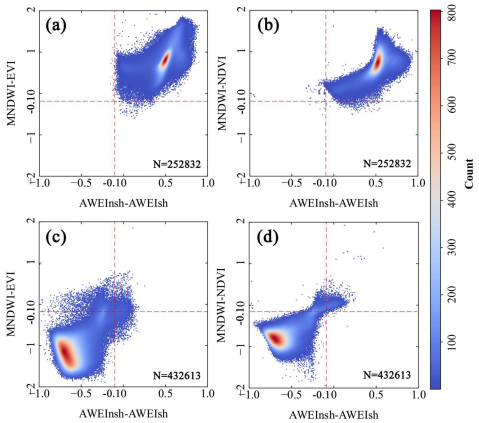

Figure 4. Density scatter of water (a-b) and non-water (c-d) samples.

2.5 Accuracy verification of water extraction based on Sentinel-2 images

In this study, 10-m spatial resolution Sentinel-2 images were used to assess the accuracy of surface water bodies acquired by the Landsat images. Considering the strong dynamic changes of surface water extent, Landsat images and Sentinel images of the same date were selected in this study, where the cloud coverage of the Landsat and Sentinel-2 images did not exceed 30%, and the same preprocessing as Landsat was applied to Sentinel-2 images, and the Sentinel-2 and Landsat surface reflectance data were finally obtained separately. Five thousand test samples were randomly generated by 15 Landsat images, including 2977 water samples and 2023 non-water samples. Sentinel-2 images were examined visually to check the test samples.

The accuracy of surface water extraction extracted by Landsat images was tested with a confusion matrix. The recognition results of Sentinel-2 images are the true values and the recognition results of Landsat images are the predicted values. First, the confusion matrix is divided into four categories: TP (true positive), FN (false negative), FP (false positive), and TN (true negative). Then, the performance of the proposed method is evaluated on this basis. For example, the producer's accuracy (PA) and user's accuracy (UA) indicators are used to indicate completeness and correctness, respectively. The accuracy (ACC) and Matthews correlation coefficient (MCC) indicate the general accuracy of the approach. The MCC considers the four confusion matrix categories and is thus more informative than the ACC, especially when the water bodies account for a small portion of the environment (Yang et al., 2020). In addition, the *KAPPA* coefficient was obtained in this study for consistency testing and can also be used to measure classification accuracy,

which usually falls between 0 and 1, and higher values indicate higher consistency (Yang et al., 2020).

2.6 Statistical Analysis

The Mann-Kendall (MK) trend test is applied to analyze time-series data with a continuous increasing or decreasing trend (monotonic trend). It is a nonparametric test that applies to all distributions (i.e., the data do not need to satisfy the assumption of a normal distribution). The MK test is used to detect significant changes in long-term permanent and seasonal water bodies (Mann 1945), and the results are interpreted in terms of a z-score metric, where the sign indicates the direction of the trend and the value indicates the magnitude of the trend. In cases where the MK test determined a significant trend, we used the coefficient of variation (CV) to analyze the spatially divergent patterns of multi-year changes in environmental factor data . Higher CV values indicate greater variation in environmental factors and less variation otherwise.

3. RESULTS

3.1 Accuracy verification of water extraction

Table 1 shows the quantitative assessment of dynamic surface water extraction results based on random sample points. The *MCC* (84.1%) and the high precision of *KAPPA* (>0.8) validate the feasibility and effectiveness of the MIWER method to obtain surface water in the study area.

samples		Landsat		
		water	non-water	Total
Sentinel-2	water	2879	98	2977
	non-water	285	1738	2023
	Total	3164	1836	5000
PA=96.7% UA=91.0%				
ACC=92.3% MCC=84.1%				
KAPPA=0.8386				

Table 1. Confusion matrix for the accuracy assessment of surface water extraction results based on random sampling points.

We selected several representative water bodies from the Yellow River basin, such as high-altitude lakes (Eling Lake) (Figure 5(a)), high-altitude reservoirs (Longyangxia Reservoir) (Figure 5(b)), desert freshwater lakes (Hongjiannao Lake) (Figure 5(c)), the Yellow River (Figure 5(d)), and low-altitude rivers and reservoirs (Dongzhang Reservior) (Figure 5(e)). Comparing with the other water body extraction algorithms, such as Deng (Figure 5(a2-e2)), SVM (Figure 5(a3-e3)), and MNDWI (Figure 5(a4-e4)), it is intuitively clear that the MIWER (Figure 5(a1-e1)) extracts water bodies better than other methods for several specific water body types. It is worth noting that the Deng and SVM methods are inferior to MIWER and MNDWI for the effects of ice, snow, and clouds on the image (Figure 5(b)).

A total of 105 sample points were visually interpreted using Sentinel-2 data as true values to evaluate the quantitative accuracy of different water body methods. The MIWER method had the highest accuracy with overall accuracy of 92.5% and KAPPA coefficient of 0.856 (Table 3), the Deng and MNDWI methods were close in accuracy, and the SVM method had the lowest accuracy.

The SVM cannot efficiently suppress the signal from built-up surfaces and using an threshold of 0 does not accurately enable discriminating built-up surfaces from water pixels (Figure 5(c3), (d3))(Xu 2006). However, the limitation of MNDWI is that it cannot discriminate water and snow (see Figure 5(a4)), because although the snow has a generally higher reflectance than the water in all the visible and infrared channels, the normalized difference between green and SWIR band for snow is as high as that of water(Choi et al., 2004; Huang et al., 2018). The Deng method, although somewhat improved over SVM and MNDWI, still has the problem of recognizing snow pixels as water pixels (Figure 5(a2)). Overall, the MIWER method has the highest accuracy and shows strong advantages for different types of water bodies.

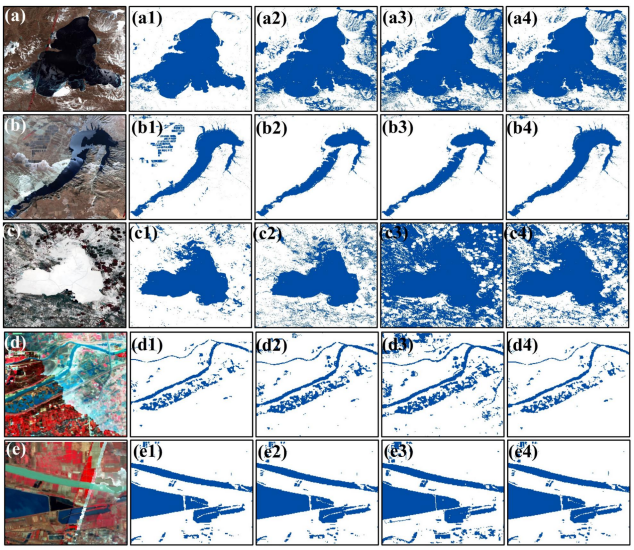

Figure 5. Comparisons between our method (a1-e1) and other methods. (a2-e2): the method of Deng et al., (2019); (a3-c3): SVM; (a4-e4): MNDWI; (a-e): false color RGB image.

Type	MIWER	Deng	SVM	MNDWI
Over accuracy	92.5%	88.5%	83.2%	86.1%
KAPPA	0.856	0.823	0.811	0.815

Table 2. Precision comparison of different water extraction methods

3.2 Temporal Distribution of the Surface Water

The annual (Figure 6(a-c)) and monthly (Figure 6(d)) variability of permanent, seasonal, and maximum water bodies (Figure 6) were investigated in this study. The MK test results showed that the inter-annual variability of surface water in YRB during 2000-2020 was more pronounced, with a significant upward trend for permanent water bodies (105.55 km^2/yr, $p<0.05$), a less pronounced inter-annual trend for seasonal water bodies ($p>0.05$), and a more pronounced inter-annual upward trend for maximum water bodies (153.04 km^2/yr, $p<0.05$). In addition, surface water has obvious seasonality: the area of the rainy season is significantly larger than that of the dry season, with the minimum extent of surface water occurring in January with a total area of 13,200.35 km^2 and the maximum extent of surface water bodies occurring in August with a total area of 15,150.08 km^2.

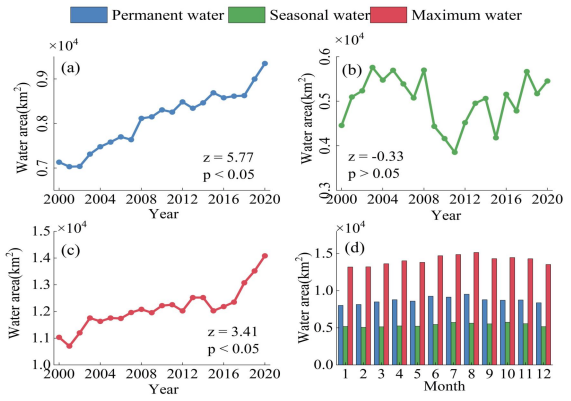

Figure 6. Annual and monthly variation of surface water in the Yellow River Basin from 2000 to 2020. The z value in the Figure 5(a-c) is the result of the MK (Mann-Kendall) test, whose symbol indicates the direction of the trend and the value indicates the magnitude of the trend. p<0.05 indicates that the MK test result is significant.

3.3 Spatial Distribution of the Open-Surface Water

Figure 7 show an overlay of all surface water extraction results in the YRB over a 20-year period, which can be used to represent the overall distribution of surface water in the YRB. The area of permanent and seasonal water bodies in the YRB is 9062.59 km^2 and 6918.83 km^2, respectively, accounting for 56.7% and 43.3% of the surface water area in the YRB, respectively. The UYRB has the largest proportion of surface water bodies at 68.6%, while the MYRB and LYRB have similar proportions at 16.6% and 14.8%, respectively. Permanent water bodies in the UYRB and MYRB account for 58.9% and 57.6%, respectively. The proportion of permanent and seasonal water bodies in the LYRB is 45.5% and 54.5%, respectively, indicating that the LYRB is dominated by seasonal water bodies. Overall, the surface water in the YRB is obviously uneven in spatial distribution and dominated by permanent water bodies; the surface water varies greatly in different regions, with the largest proportion of surface water in UYRB, and permanent water bodies dominate in UYRB and MYRB, and seasonal water bodies dominate in LYRB.

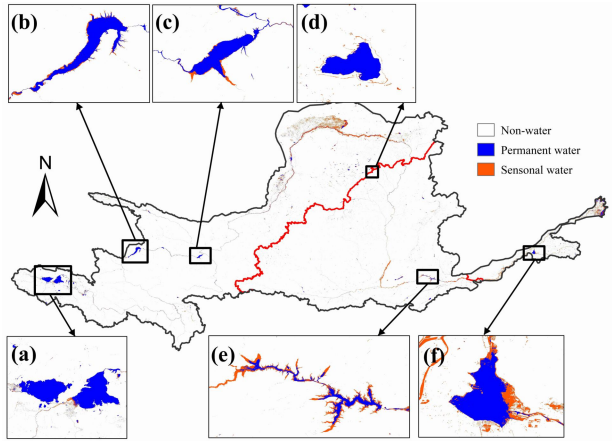

Figure 7. Spatial distribution of surface water in the YRB from 2000 to 2020. In order to view the details more obviously, some local typical water bodies are shown with enlargement. (a): Zhaling Lake and Eling Lake; (b): Longyang Reservoir; (c): Liujia Reservoir; (d): Hongjiannao Lake; (e): Xiaolangdi Reservoir; (f): Dongping Lake.

3.4 Analysis of spatial and temporal variation of lakes and reservoirs in the YRB from 2000 to 2020

The lakes and reservoirs in the YRB have changed significantly over the 20 years, with 91 new lakes and reservoirs added, 37 on a downward trend, and 66 on an upward trend (Figure 8). In the three sub-basins of YRB, lakes and reservoirs have increased, decreased, and added in different degrees. 33 lakes and reservoirs in UYRB have a decreasing trend, 54 have an increasing trend and 59 have been added; 3 lakes and reservoirs in MYRB have a decreasing trend, 3 have an increasing trend and 24 have been added; 1 lake and reservoir in LYRB has a decreasing trend, 9 have an increasing trend and 8 have been added. The results show that the changes of lakes and reservoirs in the YRB are mainly concentrated in the UYRB area, and mainly in two regions of the UYRB: the source of the Yellow River in the west and the northeastern region.

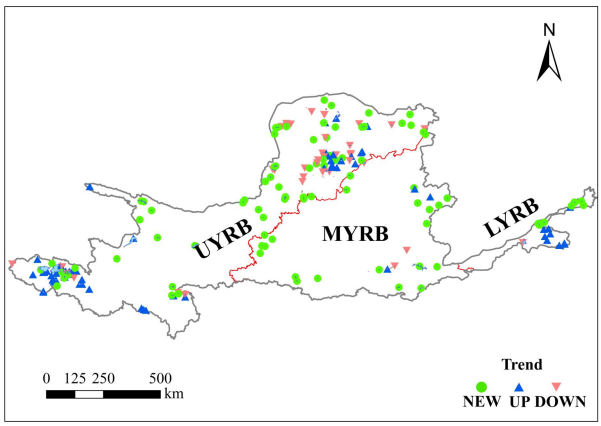

Figure 8. Spatial and temporal trends of lakes and reservoirs in the YRB from 2000 to 2020.

3.5 Conversion of different water body states in the YRB

The change of permanent and seasonal water was also counted in this study. Figure 9(a) and 10 show the conversion between non-water bodies, seasonal water bodies and permanent water bodies in the YRB. Over 20 years, the area of new permanent water bodies in the YRB is 2560.04 km^2 , of which the vast majority is from non-water bodies, accounting for 93.31%; the area of permanent water bodies that disappeared is 343.77 km^2, of which 72.40% of permanent water bodies are converted to seasonal The area of new seasonal water bodies in YRB is 6829.7km^2, of which, the vast majority is converted from non-water bodies, with a proportion of 96.35%; the area of disappeared seasonal water bodies is 1345.34km^2, of which 87.26% is converted into non-water bodies.

As shown in Figures 10(a-f), over 20 years, the surface water of Zhaling Lake almost rarely changed; Eling Lake added 74.7km^2, including 42.6km^2 of permanent water bodies and 32.1km^2 of seasonal water bodies; Longyangxia and Liujiaxia Reservoir water bodies change more similarly, the reservoir added 249.8km^2, 68.7km^2 respectively; the area of the Hongjiannao Lake decreased by 21.2km^2, 29.7% compared to 2000, with an average annual decrease of 1km^2, of which the permanent water body decreased by 15.1km^2 and the seasonal water body decreased by 6.1km^2; the main project of the Xiaolangdi Reservoir was completed in 2001 and started to store water. The reservoir area has increased by 224.3km^2, of which the permanent water has increased by 95.8km^2 and the seasonal water has increased by 128.5km^2; the area of Dongping Lake has increased by 7.3km^2 and decreased by 17.2km^2. Overall, the changes in the various lakes and reservoirs in the YRB have varied over 20 years.

This contribution has been peer-reviewed. The double-blind peer-review was conducted on the basis of the full paper.
https://doi.org/10.5194/isprs-annals-V-3-2022-9-2022 | © Author(s) 2022. CC BY 4.0 License.

The study also compared the conversion of surface water bodies in the three sub-basins from 2000 to 2020 (Figure 9(b-d)). The conversion of non-water bodies to seasonal water bodies was the largest in the UYRB, MYRB and LYRB regions with 4231.85 km^2, 1245.01 km^2 and 1071.29 km^2, respectively. The change in area of conversion of non-water bodies to permanent water bodies and conversion of seasonal water to permanent water followed closely. However, the conversion of seasonal water bodies to permanent water bodies in UYRB has the smallest area of 83.10 km^2, the conversion of permanent water bodies to non-water bodies in MYRB has the smallest area of 29.27 km^2, and the conversion of permanent water bodies to non-water bodies in LYRB has the smallest area of 9.23 km^2. In general, the conversion of surface water bodies in YRB shows a more obvious spatial heterogeneity.

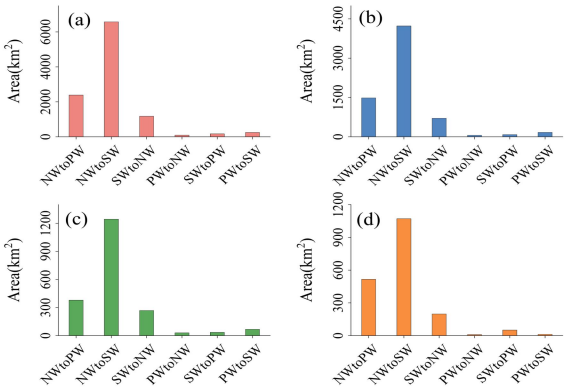

Figure 9. The conversion of open-surface water bodies in the YRB (a) and sub-basins. (b): UYRB; (c): MYRB; (d): LYRB. NW: non-water; PW: permanent water; SW: seasonal water.

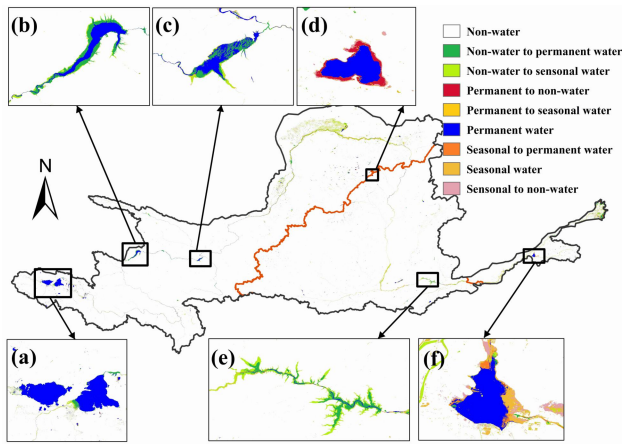

Figure 10. Spatial distribution of conversion of surface water bodies from 2000 to 2020 in the YRB. In order to view the details more obviously, some local typical water bodies are shown with enlargement. (a): Zhaling Lake and Eling Lake; (b): Longyang Reservoir; (c): Liujia Reservoir; (d): Hongjiannao Lake; (e): Xiaolangdi Reservoir; (f): Dongping Lake.

3.6 Analysis of the temporal variation of annual precipitation in YRB

Figure 11(a) shows that the annual precipitation in the YRB is unevenly distributed spatially, with precipitation decreasing from south to north. However, the multi-year precipitation in the upper and northern part of the middle reaches of the YRB shows a clear upward trend, while the eastern and lower parts of the middle reach show a clear downward trend (Figure 11(c)). From 2000 to 2020, the area with the greatest variation for annual precipitation in the YRB is the northeastern part of the UYRB, and the lowest variation for annual precipitation is found in the Yellow River headwaters area (Figure 11(b)).

Figure 11(d) shows a positive trend in annual precipitation in general (except for 2013), with a 21-year average of 480.5 mm, the highest value being 638.9 mm in 2003 and the lowest value 401.9 mm in 2001. From 2004 to 2006, the average annual precipitation in the YRB showed a decreasing trend, below the 21-year average. The average annual precipitation in 2015 decreases abruptly, and then there is a clear upward trend from 2016 to the present. In addition, the correlation between precipitation and surface water area during 2000-2020 is not strong ($p>0.05$). However, the correlation between precipitation and surface water area varies across time, with the strongest correlation of 0.92 for 2000-2003, followed by 2016-2020 with a correlation of 0.78. The weakest correlation is for 2004-2015.

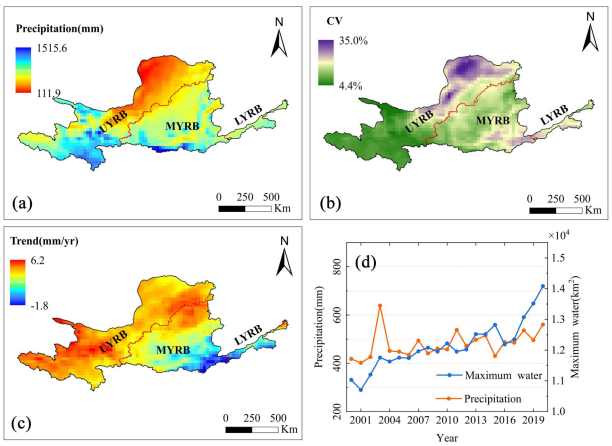

Figure 11. Interannual spatiotemporal variation of precipitation in the YRB from 2000 to 2020. (a) Spatial distribution of multi-year mean precipitation. (b) Spatial distribution of the CV (coefficient of variation) of multi-year precipitation. (c) Spatial distribution of the trend of multi-year precipitation. (d) Time-series precipitation and the maximum area of surface water.

4. DISCUSSION AND CONCLUSION

The main purpose of this study is to design an efficient method to improve the accuracy of water body extraction and to obtain long-term open surface water of the Yellow River Basin on the basis of Google Earth Engine. It includes a percentile-based image synthesis method to collect training samples and a multi-index water body extraction rule (MIWER), to rapidly extract surface water bodies. The study investigates the long-term changes of open water bodies in the YRB from 2000 to 2020 based on all available Landsat 5/7/8 images in the GEE platform. The YRB, Upper Yellow River Basin, and Middle Yellow River Basin were dominated by permanent water bodies. The permanent water bodies in the YRB increased from 2000 to 2020 as the seasonal water bodies decreased.

The maximum water body has a good correlation (over 0.6) with annual precipitation, especially the correlation between the two exceeds 0.7 for both the periods 2000-2003 and 2016-2020. The results indicate that precipitation is an important factor controlling the open surface water bodies in the YRB. In addition, precipitation across the YRB showed an increasing trend from 2000 to 2020, with more precipitation indicating more opportunities to convert non-water bodies into permanent or seasonal water bodies and seasonal water bodies into permanent water bodies. Thus, from 2000 to 2020, permanent and seasonal water bodies in the YRB increase as non-water

bodies decrease, with a conversion area of 2388.74 and 6580.85 km^2, respectively, and a smaller area of 171.30 km^2 for the conversion of seasonal water bodies to permanent water bodies. However, the precipitation trends in the different sub-basins of the YRB vary considerably (Figure 11). The UYRB experiences a significant increase in precipitation, increasing its surface water area. The MYRB experienced a slight increase, resulting in a slight increase in its surface water area. However, the LYRB experienced a decrease in precipitation, resulting in a decrease in its water body. In addition, many scholars suspect that precipitation is not the only climatic factor. For example, many studies have shown that the increase in glacial meltwater due to increasing temperatures has led to the expansion of lakes on the Tibetan Plateau, including the UYRB (Deng et al., 2019). As a result, both seasonal and permanent water bodies in the SYRB have increased from 2000 to 2020.

The correlation coefficient between maximum water bodies and annual precipitation has decreased from 2004 to 2015, possibly due to the increase in the impact of human activities on YRB in the last years. The impact of human activities on surface water bodies has been demonstrated in many studies (Zhou et al., 2019). Over the years, the YRB has experienced intense human activities that have had complex effects on surface water bodies. On the one hand, surface water bodies have been affected by human activities due to urban expansion, agricultural production, and other reasons. As an important desert freshwater lake and breeding habitat for relict gulls, the Hongjiannao wetland area has been declining overall in the last 20 years, decreasing by about 34% between 2000 and 2015. Cao et al., (2021) found that the decline in groundwater due to the continued development of nearby mines led to a continuous decrease in the area of the Hongjiannao Lake (Figure 12(c)). The area of the Hongjiannao Lake increased year by year after a series of measures such as artificial rainfall and water replenishment after 2015. On the other hand, human activities can also contribute to more surface water bodies. As an important lake at the source of the Yellow River, the water area of the Zhaling Lake and Eling Lake increased by 80km^2 in the last 20 years, and the increase of runoff into the lake is the main reason for the expansion of the water surface of the Zhaling Lake and Eling Lake (Figure 12(b)). As a key water conservancy project to manage the Yellow River, the main project of the Xiaolangdi Water Conservancy Hub was fully completed at the end of 2001. The water storage area of the Xiaolangdi Water Conservancy Hub in 2020 is increased by 114.2km^2 compared with that in 2000 (Figure 12(a)). The local government has taken a series of water conservation projects around the Fenhe Reservoir, resulting in an increase of 8 km^2 in the area of the Fenhe Reservoir in 20 years (Figure 12(d)). In the last decade, the water bodies are expected to increase as China pays more attention to water conservation of key lakes and reservoirs (Wang et al., 2018).

Generally, results obtained from this study provide the latest information for fully understanding the spatio-temporal variation of surface water body area and its driving factors for the whole Yellow River Basin, which could be used to effectively manage water resources for protecting the fragile ecology in the Yellow River Basin. The next step is to extend this method to global surface waters, which is expected to provide technical support for global water resources planning and management.

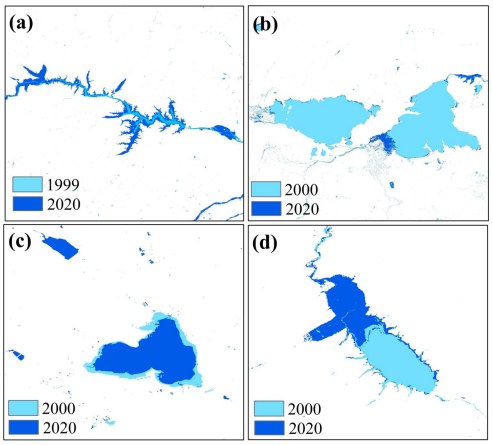

Figure 12. Typical surface water extent in the YRB in 2000 and 2020. (a): Xiaolangdi; (b): Zhaling and Eling Lake; (c): Hongjiannao Lake; (d): Fenhe Reservoir.

REFERENCES

Avtar, R., Komolafe, A.A., Kouser, A.et al., 2020: Assessing sustainable development prospects through remote sensing: A review. *Remote Sens. Appl.* 20: 100402. doi.org/10.1016/j.rsase.2020.100402.

Cao, H.Y., Han, L., Liu, Z.H.et al., 2021: Monitoring and driving force analysis of spatial and temporal change of water area of Hongjiannao Lake from 1973 to 2019. *Ecol. Inform.* 61: 101230. doi.org/10.1016/j.ecoinf.2021.101230.

Che, X.H., Feng, M., Sexton, J.et al., 2019: Landsat-Based Estimation of Seasonal Water Cover and Change in Arid and Semi-Arid Central Asia (2000–2015). *Remote Sens.* 11: 1323. doi.org/10.3390/rs11111323.

Choi, H., Bindschadler, R., 2004: Cloud detection in Landsat imagery of ice sheets using shadow matching technique and automatic normalized difference snow index threshold value decision. *Remote Sens. Environ.* 91: 237–242. doi.org/10.1016/j.rse.2004.03.007.

Claverie, M., Vermote, E.F., Franch, B.et al., 2015: Evaluation of the Landsat-5 TM and Landsat-7 ETM+ surface reflectance products. *Remote Sens. Environ.* 169: 390-403. doi.org/10.1016/j.rse.2015.08.030.

Cui, T.W., Zhang, J., Sun, L.E.et al., 2012: Satellite monitoring of massive green macroalgae bloom (GMB): imaging ability comparison of multi-source data and drifting velocity estimation. *Int. J. Remote Sens.* 33: 5513-5527. doi.org/10.1080/01431161.2012.663112

D'Odorico, P., Damm, A., Schaepman, M., 2013: Experimental Evaluation of Sentinel-2 Spectral Response Functions for NDVI Time-Series Continuity. *IEEE Trans. Geosci. Remote Sens.* 51: 1336-1348. doi.org/10.1109/TGRS.2012.2235447.

Deng, Y., Jiang, W.G., Tang, Z.H.et al., 2019: Long-Term Changes of Open-Surface Water Bodies in the Yangtze River Basin Based on the Google Earth Engine Cloud Platform. *Remote Sens.* 11: 2213. doi.org/10.3390/rs11192213.

Farr, T.G., Rosen, P.A., Caro, E.et al., 2007: The Shuttle Radar Topography Mission. *Rev. Geophys.* 45: doi.org/10.1029/2005RG000183.

Feyisa, G.L., Meilby, H., Fensholt, R.et al., 2014: Automated Water Extraction Index: A New Technique for Surface Water Mapping Using Landsat Imagery. *Remote Sens. Environ.* 140: 23–35. doi.org/10.1016/j.rse.2013.08.029.

Huang, C., Chen, Y., Zhang, S.Q.et al., 2018: Detecting, Extracting, and Monitoring Surface Water From Space Using

Optical Sensors: A Review. *Rev. Geophys.* 56: 333-360. doi.org/10.1029/2018RG000598.
Jacobs, L., Kabaseke, C., Bwambale, B.et al., 2019: The geo-observer network: A proof of concept on participatory sensing of disasters in a remote setting. *Sci. Total Environ.* 670: 245-261. doi.org/10.1016/j.scitotenv.2019.03.177.
Jay, S., Guillaume, M., 2014: A novel maximum likelihood based method for mapping depth and water quality from hyperspectral remote-sensing data. *Remote Sens. Environ.* 147: 121-132. doi.org/10.1016/j.rse.2014.01.026.
Kang, E.S., Chen, R.S., Zhang, Z.H.et al., 2007: Some Scientific problems Facing Researches on Hydrological Processes in an Inland River Basin. *Adv. Earth Sci.* 22: 940-953. doi.org/10.3321/j.issn:1001-8166.2007.09.008.
Li, H., 2021: Pattern planning and design of tiger hazelnut shrub in urban ecosystem based on remote sensing technology. *Environ. Technol. Inno.* 21: 101330. doi.org/10.1016/j.eti.2020.101330.
Lloyd, B.J., Dennison, P.E., 2018: Evaluating the response of conventional and water harvesting farms to environmental variables using remote sensing. *Agric., Ecosyst. Environ.* 262: 11-17. doi.org/10.1016/j.agee.2018.04.009.
Mann, H.B., 1945: Nonparametric tests against trend. *Econometrica: Journal of the econometric society*: 245-259. doi.org/10.2307/1907187.
McFeeters, S.K., 1996: The use of the Normalized Difference Water Index (NDWI) in the delineation of open water features. *Int. J. Remote Sens.* 17: 1425-1432. doi.org/10.1080/01431169608948714.
Meng, E.H., Huang, S.Z., Huang, Q.et al., 2019: A robust method for non-stationary streamflow prediction based on improved EMD-SVM model. *J. Hydrol.* 568: 462-478. doi.org/10.1016/j.jhydrol.2018.11.015.
Pekel, J.F., Cottam, A., Gorelick, N.et al., 2016: High-resolution mapping of global surface water and its long-term changes. *Nature* 540: 418-422. doi.org/10.1038/nature20584.
Rao, P.Z., Jiang, W.G., Hou, Y.K.et al., 2018: Dynamic Change Analysis of Surface Water in the Yangtze River Basin Based on MODIS Products. *Remote Sens.* 10: 1025. doi.org/10.3390/rs10071025.
Rudorff, N., Rudorff, C.M., Kampel, M.et al., 2018: Remote sensing monitoring of the impact of a major mining wastewater disaster on the turbidity of the Doce River plume off the eastern Brazilian coast. *ISPRS J. Photogramm. Remote Sens.* 145: 349-361. doi.org/10.1016/j.isprsjprs.2018.02.013.
Urban, A., Di Napoli, C., Cloke, H.L.et al., 2021: Evaluation of the ERA5 reanalysis-based Universal Thermal Climate Index on mortality data in Europe. *Environ. Res.* 198: 111227. doi.org/10.1016/j.envres.2021.111227.
Vermote, E., Justice, C., Claverie, M.et al., 2016: Preliminary analysis of the performance of the Landsat 8/OLI land surface reflectance product. *Remote Sens. Environ.* 185: 46-56. doi.org/10.1016/j.rse.2016.04.008.
Vörösmarty, C., McIntyre, P., Gessner, M.et al., 2010: Global threats to human water security and river biodiversity. *Nature* 467: 555-561. doi.org/10.1038/nature09440.
Wang, C., Jia, M.M., Chen, N.C.et al., 2018: Long-Term Surface Water Dynamics Analysis Based on Landsat Imagery and the Google Earth Engine Platform: A Case Study in the Middle Yangtze River Basin. *Remote Sens.* 10: 1635. doi.org/10.3390/rs10101635.
Wang, Y.B., Ma, J., Xiao, X.M.et al., 2019: Long-Term Dynamic of Poyang Lake Surface Water: A Mapping Work Based on the Google Earth Engine Cloud Platform. *Remote Sens.* 11: 313. doi.org/10.3390/rs11030313.
Xu, H.Q., 2006: Modification of normalised difference water index (NDWI) to enhance open water features in remotely sensed imagery. *Int. J. Remote Sens.* 27: 3025-3033. doi.org/10.1080/01431160600589179.
Yang, X.C., Qin, Q.M., Hervé, Y.et al., 2020: Monthly estimation of the surface water extent in France at a 10-m resolution using Sentinel-2 data. *Remote Sens. Environ.* 244: 111803. doi.org/10.1016/j.rse.2020.111803.
Yu, H., Shui, P.L., Lu, K., 2021: Outlier-robust tri-percentile parameter estimation of K-distributions. *Signal Process.* 181: 107906. doi.org/10.1016/j.sigpro.2020.107906.
Zhang, Z.X., Ming, D.P., Xing, T.Y., 2011: Eco-environmental Monitoring and Evaluation of the Tekes Watershed in Xinjiang Using Remote Sensing Images. *Procedia Environ. Sci.* 10: 427-432. doi.org/10.1016/j.proenv.2011.09.070.
Zhou, Y., Dong, J.W., Xiao, X.M.et al., 2019: Continuous monitoring of lake dynamics on the Mongolian Plateau using all available Landsat imagery and Google Earth Engine. *Sci. Total Environ.* 689: 366-380. doi.org/10.1016/j.scitotenv.2019.06.341.
Zhu, C.M., Li, J.L., Zhang, X.et al., 2015: BostenWater Resource Dynamic Detection and Feature Analysis in Recent 40 Years by Remote Sensing. *Journal of Natural Resources* 30: 106-114. doi.org/10.11849/zrzyxb.2015.01.009.
Zou, Z.H., Xiao, X.M., Dong, J.W.et al., 2018: Divergent trends of open-surface water body area in the contiguous United States from 1984 to 2016. *Proc. Natl. Acad. Sci.* 115: 3810. doi.org/10.1073/pnas.1719275115.